Automotive Science and Engineering, Vol. 16, No. 4, (2026), 5208-5223

Iran University of Science and Technology

Automotive Science and Engineering

Journal Homepage: ase.iust.ac.ir

ISSN: 2008-9899

Comparative Energy and Hydrogen Performance of a Fuel-Cell Electric Vehicle Across Standard Driving Cycles

Amir Ansari Laleh[1], Mohammad Hasan Shojaeefard[2*]

[1] Ph.D. Student, Mechanical Engineering, Iran University of Science and Technology, Tehran, Iran.

[2] Professor, Mechanical Engineering, Iran University of Science and Technology, Tehran, Iran.

ARTICLE INFO

Article history:

Received : 30 Feb 2026

Accepted: 14 Sep 2026

Published: 7 Oct 2026

Keywords:

Fuel-cell electric vehicle

Hydrogen consumption

Driving cycle

Energy management strategy

A B S T R A C T

The performance of fuel-cell electric vehicles (FCEVs) depends not only on stack efficiency but also on the dynamic interaction among hydrogen conversion, battery buffering, and vehicle-level power demand, which is strongly shaped by the imposed driving cycle. This study develops a forward-facing, multi-domain system-level model of a Toyota-Mirai-type FCEV in Simcenter Amesim, integrating the hydrogen storage and PEM fuel-cell subsystem, balance-of-plant auxiliaries, high- and low-voltage electrical buses, traction battery, power electronics, drivetrain, and a rule-based, stack-led energy-management strategy. Three standardized driving schedules WLTC, NEDC, and UDDS were simulated under identical powertrain parameters and initial conditions (80% initial SOC, ~5.0 kg hydrogen) to isolate the effect of driving-cycle dynamics on energy flow. Results show that the fuel-cell stack consistently supplies the base-load propulsion power, while the battery absorbs all regenerative-braking energy and covers transient peaks, never allowing reverse power into the stack. Although absolute hydrogen consumption and mean stack power varied substantially across cycles (166.52 g for WLTC versus 83.34 g for NEDC), the distance-normalized hydrogen economy converged to a narrow band of 0.748–0.781 kg H2/100 km, and peak stack power remained within 31.6–37.0 kW for all cases. These findings demonstrate that the stack-led energy-management strategy achieves cycle-independent efficiency and robust component utilization, providing a validated baseline for future optimization and degradation-aware control studies.

1. Introduction

The transition toward low-carbon transportation has intensified research on powertrain technologies capable of combining high energy efficiency, low local emissions, extended driving range, and operational flexibility[1]. Among the available electrified propulsion concepts, proton-exchange-membrane fuel-cell electric vehicles (FCEVs) represent a promising pathway because hydrogen can be converted electrochemically into electricity while retaining the fast-refuelling capability traditionally associated with conventional vehicles. However, the practical performance of an FCEV is determined not only by the efficiency of the fuel-cell stack but also by the dynamic interaction among hydrogen conversion, auxiliary loads, electrical energy storage, regenerative braking, power electronics, and vehicle-level power demand. Consequently, FCEV performance should be evaluated as an integrated energy-conversion and management

*Corresponding Author
Email Address: shojaeefard@iust.ac.ir
https://doi.org/10.22068/ase.2026.757

"*Automotive Science and Engineering*" is licensed under a Creative Commons Attribution-Noncommercial 4.0 International License.

[Downloaded from rds.iust.ac.ir on 2026-11-15]

problem rather than as the isolated operation of the fuel-cell stack [2], [3].

In most automotive fuel-cell architectures, the proton-exchange-membrane fuel cell (PEMFC) provides the dominant share of the propulsion energy, whereas a high-voltage battery compensates for the comparatively slow transient response of the stack. The battery supplies or absorbs power during rapid load variations and captures energy during regenerative braking. Hybridization therefore creates a coupled energy-conversion chain in which the chemical energy stored in hydrogen is converted into electrical energy, distributed through DC buses and power-electronic converters, and ultimately transformed into mechanical traction energy. The instantaneous operating points of the fuel cell and battery are governed by the energy-management strategy (EMS), making power allocation a major determinant of hydrogen consumption, battery state of charge (SOC), regenerative-energy utilization, and fuel-cell loading [4], [5].

The Toyota Mirai has become an important benchmark platform for investigating fuel-cell/battery interaction and vehicle-level energy management. Carignano and Costa-Castelló [5] developed a low-order powertrain model of the Toyota Mirai and reconstructed a rule-based EMS using experimental information. Their comparison with dynamic-programming solutions indicated that the production-oriented strategy operated relatively close to the optimum in terms of fuel economy, while larger opportunities remained for reducing stress on the fuel cell and battery. Usmanov et al. [6] similarly developed and validated a Toyota-Mirai-based FCHEV model and compared a rule-based controller with an equivalent consumption minimization strategy. Their results showed that the benefit of control optimization depends on the driving cycle, emphasizing that hydrogen economy cannot be assessed independently of the imposed duty profile.

Driving-cycle characteristics are particularly important because vehicle speed and acceleration continuously modify inertial, rolling-resistance, and aerodynamic loads and consequently alter both the magnitude and dynamics of the required traction power. Urban cycles characterized by frequent stop-and-go operation generate repeated transient power demands and regenerative-braking opportunities, whereas higher-speed operation increases aerodynamic losses and may impose sustained fuel-cell loading. Agati et al. [7] showed that the degree of hybridization and the adopted EMS affect hydrogen consumption, battery stress, overall efficiency, and predicted fuel-cell lifetime. Changizian et al. [8] likewise demonstrated, using several conventional driving cycles, that regenerative braking, battery SOC management, and hybrid energy-storage configuration can materially influence hydrogen consumption and vehicle performance. These findings indicate that evaluation under a single driving schedule may not adequately characterize the interaction between powertrain architecture and supervisory control.

A large body of research has therefore focused on increasingly sophisticated power-management approaches. Optimization-based methods, adaptive control, model-predictive control, and learning-based strategies have been proposed to reduce hydrogen consumption while limiting rapid fuel-cell load variation and maintaining battery SOC within a desired range. Sun et al. [9] developed an AMESim-based FCEV model and used it to evaluate an adaptive EMS that explicitly balanced fuel economy and fuel-cell durability. More recently, Islam et al. [10] proposed a six-step supervisory strategy for a fuel-cell/battery/supercapacitor hybrid powertrain under a real-world driving cycle, further illustrating the trend toward multi-source and condition-dependent energy management. Although such approaches can improve selected performance indicators, their increasing algorithmic complexity can make it difficult to distinguish gains arising from the controller itself from those caused by fundamental differences in driving demand and energy-conversion conditions. A physically transparent system-level baseline is therefore valuable before additional optimization layers are introduced.

System-level simulation provides an effective means of establishing such a baseline because mechanical, electrical, thermal, and fluidic processes can be represented within a common computational framework. In addition to the AMESim-based work of Sun et al. [9], Iqbal et al. [11] developed a high-fidelity data-driven powertrain model inspired by the Toyota Mirai and investigated nonlinear interactions between the fuel-cell system and traction battery under combined NEDC, WLTP, and US06 operating profiles. Such studies demonstrate that realistic assessment of an FCHEV requires more than a static efficiency representation; it requires a dynamic description of the power flows linking the fuel-cell stack, balance-of-plant auxiliaries, electrical storage system, drivetrain, and vehicle longitudinal dynamics.

[Downloaded from rds.iust.ac.ir on 2026-11-15]

Hydrogen utilization is another central indicator of the overall conversion process. Because fuel-cell efficiency varies with operating point, total hydrogen use cannot be inferred reliably from travelled distance or average traction power alone. Da Silva et al. [12] developed an analytical framework for estimating hydrogen consumption in a Toyota-Mirai-based hybrid powertrain and validated it against roller-test-bench measurements over several homologation cycles, reporting an overall root-mean-square error below 4%. Experimental work on the second-generation Toyota Mirai by Alves et al. [13] further showed that stack- and system-level efficiencies vary substantially with load and reported a WLTC hydrogen consumption of approximately 0.8 kg H2/100 km. These findings underline the need to interpret hydrogen economy together with the corresponding power-flow history rather than as an isolated aggregate metric.

Recent on-road measurements also confirm the central role of the traction battery in determining FCEV energy flow. Cieślik et al. [14] examined the second-generation Toyota Mirai under real driving conditions and observed substantial differences in fuel-cell contribution, high-voltage battery cycling, regenerative-energy recovery, and hydrogen use between operating modes. The battery should therefore be regarded as an active dynamic buffer rather than simply an auxiliary energy source. Accordingly, a meaningful system-level evaluation should simultaneously consider fuel-cell power, battery power, SOC evolution, regenerative operation, hydrogen depletion, and the resulting vehicle-level energy economy.

Despite these advances, much of the existing literature has concentrated on developing or optimizing a specific EMS, sizing hybrid energy-storage components, or validating performance under one or a limited combination of driving schedules. Comparatively fewer studies isolate the influence of driving-cycle dynamics through a controlled, like-for-like system-level comparison in which the powertrain configuration, supervisory logic, component parameters, hydrogen inventory, and initial battery SOC are held constant while fundamentally different standardized cycles are imposed. In addition, cycle-dependent studies often report hydrogen consumption or SOC separately, whereas the coupled evolution of traction demand, fuel-cell output, battery buffering, regenerative-energy absorption, hydrogen depletion, normalized hydrogen economy, and remaining driving range is less frequently examined within a single multi-domain framework. This limits the ability to determine whether apparently favorable energy performance is intrinsic to the conversion architecture and control philosophy or is primarily a consequence of the selected driving schedule.

To address this gap, the present study develops a forward-facing, multi-domain system-level representation of a Toyota-Mirai-type FCEV in Simcenter Amesim. The model integrates the hydrogen storage and supply system, PEM fuel-cell stack, balance-of-plant auxiliaries, cooling circuit, high- and low-voltage electrical buses, traction battery, power-electronic converters, electric drivetrain, vehicle longitudinal dynamics, and supervisory control within a unified energy-flow architecture. Three standardized driving schedules with substantially different dynamic characteristics the Worldwide Harmonized Light-Duty Vehicles Test Cycle (WLTC), New European Driving Cycle (NEDC), and Urban Dynamometer Driving Schedule (UDDS) are imposed under identical powertrain parameters and initial conditions. The principal contribution is a controlled multi-cycle assessment of the energy-conversion and power-management behavior of an integrated fuel-cell/battery vehicle architecture, with particular attention to fuel-cell and battery power response, battery buffering and regenerative-energy absorption, SOC evolution, cumulative and distance-normalized hydrogen consumption, and estimated driving range. The resulting framework provides a physically interpretable baseline for assessing cycle sensitivity and the robustness of stack-led FCEV energy management, while also establishing a foundation for subsequent optimization, degradation-aware control, and real-world operating studies.

2. Methodology

This section presents the system-level methodology used to evaluate the dynamic and energetic behaviour of a Toyota Mirai fuel-cell electric vehicle (FCEV) under standardized driving conditions. The framework combines a forward-facing Simcenter Amesim model, longitudinal vehicle dynamics, a proton-exchange-membrane fuel-cell (PEMFC) and hydrogen subsystem, a traction battery, and a rule-based power-management strategy. Three reference driving cycles WLTC, NEDC, and UDDS were applied independently under identical initial conditions. The resulting time-series signals were then post-processed to quantify vehicle power demand, fuel-cell and battery power sharing, hydrogen consumption, battery state of charge (SOC), and remaining driving range.

[Downloaded from rds.iust.ac.ir on 2026-11-15]

2.1 System Architecture and Forward-Facing Vehicle Model

The propulsion system was represented by a forward-facing, multi-domain model implemented in Simcenter Amesim 2404. The model couples the mechanical, electrical, thermal, and fluidic domains required to reproduce the principal energy flows of the FCEV. In the forward-facing configuration, the prescribed driving-cycle speed is treated as a reference rather than an imposed vehicle state: a closed-loop driver model generates the propulsion command required to minimize the speed-tracking error, and the achieved vehicle speed emerges from the response of the powertrain and longitudinal vehicle dynamics.

As shown in Fig. 1, the model comprises three interacting subsystems. The fuel-cell/hydrogen subsystem includes a compressed-hydrogen storage tank, a PEM fuel-cell stack, and balance-of-plant (BoP) auxiliaries representing loads associated with the air compressor, humidification system, and coolant pumps. The electrical/drivetrain subsystem contains the DC bus and converters, traction battery, traction inverter, and electric motor. The vehicle/control subsystem consists of the longitudinal vehicle-dynamics block, the driver controller, and the reference driving-cycle input. The traction battery exchanges power bidirectionally with the DC bus, allowing it to support transient propulsion demand and absorb regenerative-braking energy.

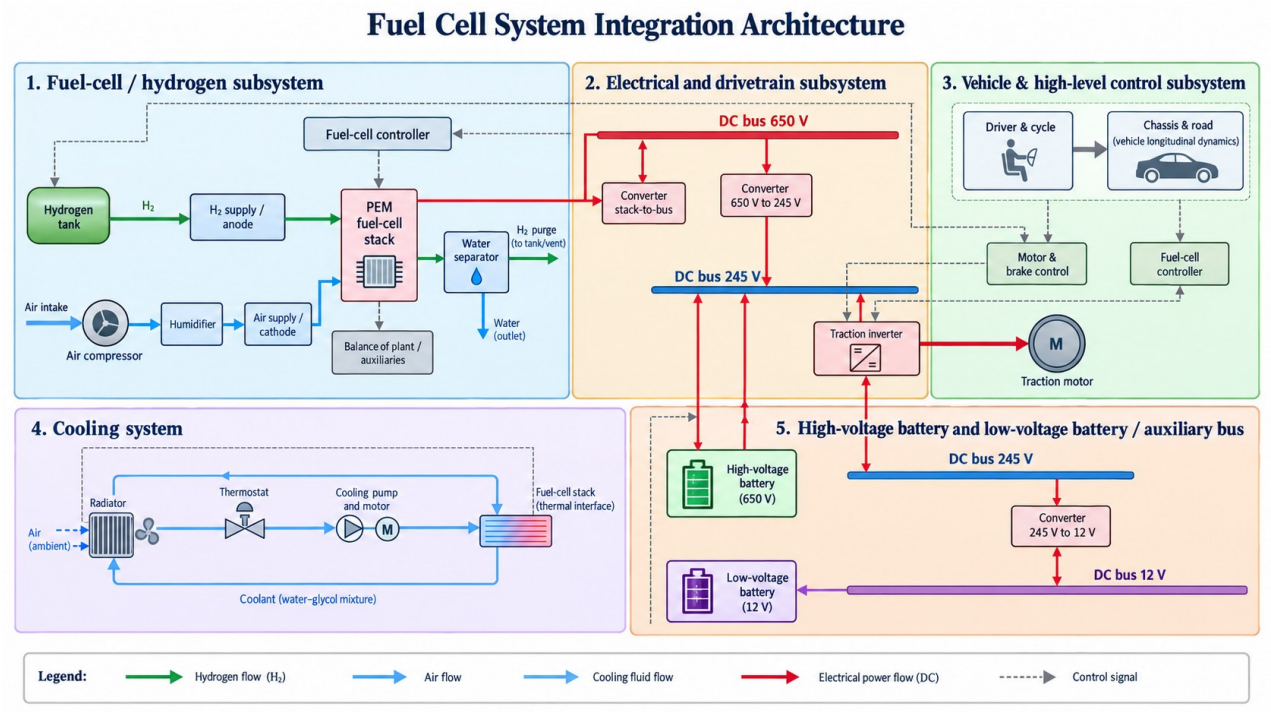


Figure 1: Schematic architecture of the simulated fuel-cell/battery hybrid powertrain and its principal power- and signal-flow paths.

[Downloaded from rds.iust.ac.ir on 2026-11-15]

All driving-cycle simulations used the same component parameterization and initial states. This common setup was maintained to ensure that the differences reported among the three cases are attributable to the imposed driving-cycle characteristics rather than changes in vehicle configuration. The analysis is intentionally performed at system level; therefore, internal electrochemical submodels embedded within the Amesim PEMFC component are not reformulated beyond the governing power and hydrogen-flow relations required for the present energy analysis.

2.2 Longitudinal Vehicle Dynamics and Traction-Power Demand

The vehicle power demand is determined by the longitudinal force balance. At each time instant, the tractive force must overcome the inertial, rolling-resistance, aerodynamic-drag, and road-grade components. The total force requirement can be expressed as [15]:

$$F_{trac}(t) = F_{in}(t) + F_{roll}(t) + F_{aero}(t) + F_{grade} \quad (1)$$

where the inertial contribution is

$$F_{in}(t) = m \cdot dv(t)/dt \quad (2)$$

the rolling-resistance force is

$$F_{roll}(t) = mgC_r cos(\theta) \quad (3)$$

the aerodynamic-drag force is

$$F_{aero}(t) = ½\rho air C_d A f_v(t) \quad (4)$$

and the grade-resistance force is

$$F_{grade}(t) = mgsin(\theta) \quad (5)$$

Here, m is the vehicle mass, g is gravitational acceleration, $C_r$is the rolling-resistance coefficient, ρ_{air} is air density, $C_d$is the aerodynamic drag coefficient, $A_f$is the frontal area, and θ is the road inclination angle. For level-road cycle simulations, the grade term vanishes when θ = 0. The instantaneous mechanical power at the wheels is consequently

$$P_{wheel}(t) = F_{trac}(t) \cdot v(t) \quad (6)$$

Positive wheel power corresponds to propulsion demand, whereas negative wheel power during deceleration represents mechanical energy that can potentially be recovered through regenerative braking. This formulation explains why differences in speed, acceleration severity, and stop-and-go frequency among the driving cycles directly affect fuel-cell loading, battery utilisation, and hydrogen consumption.

2.3 Driving Cycles and Driver Model

Three standardized chassis-dynamometer cycles were selected to provide distinct operating envelopes: the Worldwide Harmonized Light-Duty Vehicles Test Cycle (WLTC), the New European Driving Cycle (NEDC), and the Urban Dynamometer Driving Schedule (UDDS). Their nominal characteristics are summarized in Table 1. The cycles differ substantially in duration, transient severity, speed distribution, and frequency of acceleration and braking, thereby providing a suitable basis for comparing the behaviour of the fuel-cell/battery powertrain under mixed, structured, and urban stop-and-go operation[16].

Table 1: Nominal characteristics of the reference driving cycles used as simulation inputs.

Driving cycle	Nominal distance (km)	Nominal duration (s)	Maximum speed (km/h)	Representative operating condition
WLTC	23.25	1800	131.3	Mixed urban, extra-urban, and motorway operation
NEDC	11.01	1180	120.0	Legacy European urban and extra-urban type-approval cycle
UDDS	12.07	1369	91.2	Urban, stop-and-go driving

For each case, the reference speed $v_{ref}(t)$was provided to a PI-type driver controller. The controller converted the instantaneous speed-tracking error into the propulsion command required to follow the prescribed trajectory. The acceleration associated with the realized vehicle speed can be written as

$$a(t) = dv(t)/dt \quad (7)$$

[Downloaded from rds.iust.ac.ir on 2026-11-15]

or, for the discretely logged simulation data, approximated by

$$ai \approx [vi - vi - 1]/[ti - ti - 1] \quad (8)$$

Each cycle was executed as an independent simulation experiment using the same initial hydrogen inventory and battery SOC. Because the model is forward-facing, the achieved speed and distance may differ slightly from the nominal reference values when the driver-powertrain system cannot perfectly reproduce a rapid reference transition. For this reason, nominal cycle specifications are reported in Table 1, whereas the actual reproduced distance, speed, and duration used in the performance calculations are obtained directly from the simulated vehicle signals.

2.4 PEM Fuel-Cell and Hydrogen Subsystem

The PEM fuel-cell stack is the primary onboard energy-conversion device. Hydrogen is supplied from the high-pressure storage tank to the fuel-cell subsystem, while the generated electrical power is transferred to the DC bus after accounting for the electrical demand of the balance-of-plant auxiliaries. At system level, the gross electrical power produced by the stack is

$$P_{stack}(t) = V_{stack}(t) \cdot I_{stack}(t) \quad (9)$$

where V_{stack} and I_{stack} are the instantaneous stack voltage and current, respectively. The net fuel-cell-system power available to the electrical bus can be expressed as

$$P_{FC,net}(t) = P_{stack}(t) - P_{BoP}(t) \quad (10)$$

where P_{BoP} represents the combined parasitic electrical demand of the auxiliary devices represented in the model. The instantaneous energy-conversion efficiency may be defined on a lower-heating-value basis as

$$\eta_{FC}(t) = P_{FC,net}(t)/[\dot{m}_{H2}(t) \cdot LHV_{H2}] \quad (11)$$

where $\dot{m}_{H2}$ is the hydrogen mass-flow rate and LHV_{H2} is the lower heating value of hydrogen. In the present work, hydrogen flow and remaining tank mass were obtained directly from the Amesim fuel-cell/hydrogen subsystem rather than reconstructed solely from traction power. The cumulative hydrogen mass consumed during a cycle is therefore

$$m_{H2,cons} = \int_0^T \dot{m}_{H2}(t)dt \quad (12)$$

and is equivalently obtained from the difference between the initial and final hydrogen-tank masses. This approach retains the influence of the modeled fuel-cell and auxiliary-system behaviour on the reported hydrogen consumption.

2.5 Traction Battery and State of Charge

The traction battery acts as a bidirectional energy buffer. It supplements the fuel-cell system when rapid or high-amplitude propulsion demand exceeds the preferred stack response and stores energy recovered during deceleration. For interpretation of the battery state, the SOC follows the conventional charge-balance definition

$$SOC(t) = SOC_0 - (1/Q_{nom}) \int_0^t I_{bat}(\tau)d\tau \quad (13)$$

where SOC_0 is the initial battery state of charge, Q_{nom} is the nominal charge capacity, and I_bat is the battery current under the adopted sign convention. The equivalent differential form is

$$dSOC/dt = -I_{bat}(t)/Q_{nom} \quad (14)$$

The SOC used in the analysis was logged directly from the battery state-estimation block of the Amesim model. An initial SOC of 80% was used for all three driving-cycle simulations. The sign convention adopted in the reported power traces assigns negative battery power to battery charging; accordingly, regenerative-braking events appear as negative battery-power excursions.

2.6 Energy-Management and Power-Split Strategy

Power sharing between the fuel-cell system and traction battery follows a rule-based, stack-led strategy. The fuel-cell system is used as the primary source for the base-load component of propulsion demand, while the battery compensates rapid load fluctuations and short-duration peak-power events. At the DC-bus level, the power balance can be written conceptually as

[Downloaded from rds.iust.ac.ir on 2026-11-15]

$$P_{dem}(t) = P_{FC,net}(t) + P_{bat}(t) - P_{conv,loss}(t) \quad (15)$$

where $P_{dem}$is the electrical power required by the propulsion system and auxiliaries, $P_{bat}$is the battery power, and $P_{conv,loss}$represents aggregate converter and drivetrain electrical losses not already embedded in the component signals. Under positive traction demand, the fuel-cell system supplies the dominant share of the requested power and the battery provides transient support when required.

During braking and deceleration, the traction path can operate regeneratively. Because the fuel-cell stack cannot accept reverse electrical power, recovered braking energy is routed to the traction battery. With the sign convention used in the simulation outputs, regenerative operation is characterized by negative battery power. This division of roles limits rapid stack load cycling while preserving the battery as the principal short-term power buffer.

2.7 Simulation Setup and Data Acquisition

All simulations were carried out in Simcenter Amesim 2404 using the software's built-in variable-step numerical integration. A common simulation window of 1800 s was used for the three experiments. For the shorter NEDC and UDDS cases, the vehicle remained at rest after completion of the prescribed reference cycle. Model outputs were recorded at a fixed interval of 2 s, producing 901 time-stamped samples per run.

The logged variables included reference and achieved vehicle speed, traction power, fuel-cell stack power, BoP power, battery power, hydrogen mass-flow rate, remaining hydrogen mass, battery SOC, and estimated vehicle range. These signals form the basis of all derived quantities and comparisons presented in the Results and Discussion section.

2.8 Post-Processing and Performance Indicators

The raw time-series data exported from Amesim were processed in Python using pandas and NumPy. Derived quantities were calculated from the logged signals using the same procedure for each driving cycle.

Table 2: Main simulation settings and common initial conditions.

Setting	Value / implementation
Simulation platform	Simcenter Amesim 2404
Numerical integration	Built-in variable-step solver
Common simulation window	1800 s
Logged output interval	2 s
Samples per simulation	901
Initial hydrogen inventory	Approximately 5.0 kg
Hydrogen storage pressure	700 bars
Initial battery SOC	80%
Driving-cycle experiments	WLTC, NEDC, UDDS

The actual distance travelled was obtained by numerical integration of the achieved vehicle speed over the active cycle duration:

$$D = \int_0^T v(t)dt \quad (16)$$

The integral was evaluated numerically using the trapezoidal rule. Hydrogen economy was normalized by the simulated distance according to

$$HE = \left[m_{H2,cons}/D\right] \times 100 \quad (17)$$

where HE is expressed in kg H2/100 km when $m_{H2,cons}$ is given in kilograms and D in kilometres. This normalization permits a direct comparison among cycles of different length and duration.

The net battery-SOC change was calculated as

$$\Delta SOC = SOC_{final} - SOC_{initial} \quad (18)$$

and the mean and peak fuel-cell stack powers were obtained from

$$P_{stack} = (1/T)\int_0^T P_{stack}(t)dt \quad (19)$$

[Downloaded from rds.iust.ac.ir on 2026-11-15]

$$P_{stack,peak} = max[P_{stack}(t)] \quad (20)$$

Cumulative hydrogen consumption, SOC excursions, and the corresponding power trajectories were evaluated over the active portion of each driving cycle. The reported remaining-range signal was taken directly from the model's range-estimation block, which projects the remaining driving distance from the current hydrogen inventory and a receding-window estimate of recent specific hydrogen consumption. Because this estimator requires an initial convergence period, the first 120 s were excluded from the range plots and range-based interpretation to avoid non-physical start-up transients.

2.9 Comparative Evaluation Procedure

The three driving-cycle cases were compared using the same set of indicators: achieved distance and speed response, traction/fuel-cell/battery power histories, cumulative hydrogen consumption, hydrogen economy, battery SOC evolution, mean and peak stack power, and estimated remaining range. The use of identical initial conditions and an identical post-processing procedure provides a like-for-like basis for assessing how driving-cycle severity modifies energy flow and component utilization. No cycle-specific retuning of the vehicle or powertrain parameters was introduced between the three experiments.

2.10 Model Validation Against Toyota Mirai Test Data

The forward-facing Amesim model was checked against public chassis-dynamometer measurements of a Toyota Mirai (first generation) from the Downloadable Dynamometer Database (D3) of Argonne National Laboratory. Two independent hot-start UDDS tests (IDs 61712009 and 61712011, ambient 21–22 °C) were used as the experimental reference, because the UDDS is the only cycle of the present study with a measured Mirai counterpart. The UDDS simulation was compared with no re-tuning of any model parameter. The measured signals were time-aligned with the simulation by cross-correlating vehicle speed (r = 0.999) and interpolated onto the 2-s output grid. Errors were evaluated over the 1370-s UDDS schedule. Figure 2 compares vehicle speed, stack power, battery power, SOC change and cumulative hydrogen consumption. The driver model tracks the measured speed trace with a root-mean-square error (RMSE) of 0.93 km/h (R^2 = 0.998), so both tests and the simulation impose practically the same traction demand (Fig. 2a). The stack-power response is reproduced in timing and magnitude (Fig. 2b): the correlation coefficient with the measurements is r = 0.85–0.86 and the RMSE is 3.1 kW (about 10 % of the measured range). The simulated peak stack power of 36.5 kW is 6–11 % higher than the measured peaks (32.9–34.4 kW). The model also captures the regenerative-braking charging peaks of the battery (Fig. 2c), but it supplies less battery discharge power during accelerations than the production vehicle. Over the cycle, battery discharge energy is 0.34 kWh in the model versus 0.70–0.73 kWh in the tests.

The cumulative hydrogen consumption follows the measured trend closely (r = 0.998, Fig. 2e), but the cycle-end value is higher: 93.6 g versus 75.2–76.9 g, i.e. 0.787 versus 0.626–0.640 kg H2/100 km. After a charge-balance correction for the net change in battery energy, the difference is about 19 %. This difference is not caused by the fuel-cell submodel. When the simulated hydrogen flow is compared with the steady-state hold points of the Mirai fuel-cell mapping test (ANL 61712049), the two agree within −1.2 % to +3.8 % between 10.6 and 32 kW. The difference arises at the energy-management level. The rule-based, stack-led strategy keeps the stack at about 1.7 kW during vehicle stops, whereas the production vehicle uses fuel-cell idle-stop (Fig. 2b). It also makes less use of the battery during accelerations. As a result, the simulated stack delivers 1.93 kWh over the cycle, compared with 1.62–1.63 kWh in the tests.The relative SOC trajectory (Fig. 2d) reproduces the direction and timing of the measured excursions during the first five minutes of the cycle: charging on the first decelerations and depletion during the semi-highway segment. Afterwards, the simulated SOC settles 3–7 percentage points above the measurements and ends the cycle at +5.6 pp, compared with +2.0 and −1.5 pp in the two tests.

[Downloaded from rds.iust.ac.ir on 2026-11-15]

This deviation is expected. The simulation starts at 80 % SOC, whereas the vehicle operated at 57–61 %, and the implemented rule-based strategy is not a reproduction of Toyota's proprietary control. The two repeat tests themselves differ by up to 4 pp in SOC, so the SOC path of the production controller is not unique even for the same cycle.

Overall, the model is validated for vehicle speed tracking, for stack-level hydrogen conversion, and for the timing and magnitude of the stack and battery power response. The absolute hydrogen economies reported in Section 3 should be read as conservative (upper-bound) values relative to the production Mirai control. They are consistent in magnitude with the approximately 0.8 kg H2/100 km reported for the WLTC by Alves et al. [13]. The SOC trajectories are a property of the implemented energy-management strategy and are used here for the comparison between cycles, not as a prediction of the production vehicle's battery operation.

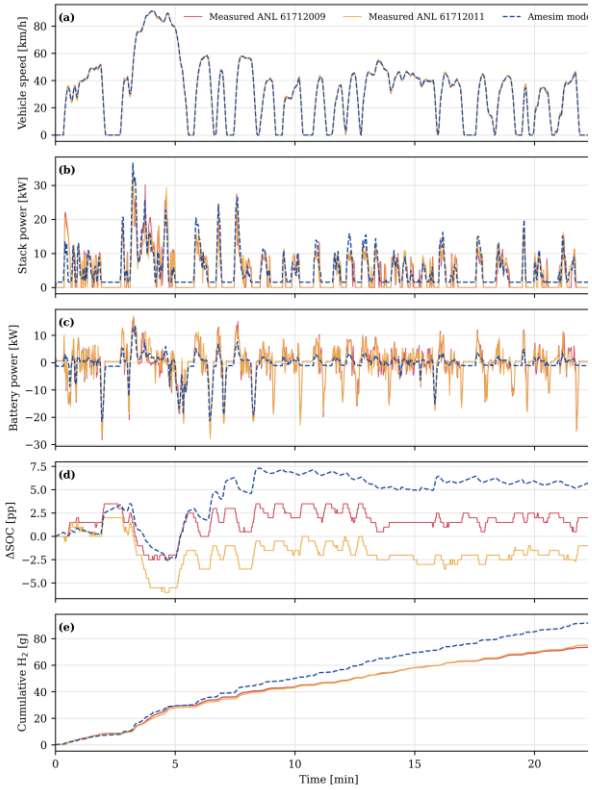


Figure 2: Validation of the Amesim model over the UDDS against two measured Toyota Mirai (Gen 1) chassis-dynamometer tests (ANL D3, tests 61712009 and 61712011): (a) vehicle speed, (b) fuel-cell stack power, (c) battery power (negative = charging), (d) change of battery SOC from the start of the cycle, and (e) cumulative hydrogen consumption. No model parameter was re-tuned.

3. Results

The simulated fuel-cell propulsion system of the Toyota Mirai, implemented in Simcenter Amesim, was exercised over three standard driving cycles the Worldwide Harmonized Light-Duty Vehicles Test Cycle (WLTC), the New European Driving Cycle (NEDC), and the Urban Dynamometer Driving Schedule (UDDS) to evaluate the dynamic behaviour of the stack, battery, and hydrogen-consumption subsystems under distinct load profiles. Table 1 summarises the main characteristics of the three cycles together with the key simulation outputs; the following subsections analyse these results in detail with reference to Figs. 1–6.

Table 3: Summary of driving-cycle characteristics and key simulation results.

Parameter	WLTC	NEDC	UDDS
Effective duration (min)	30.0	19.5	22.7
Maximum speed (km/h)	108.1	120.0	91.2
Distance travelled (km)	22.25	10.92	11.99
Hydrogen consumed (g)	166.52	83.34	93.64
Hydrogen economy (kg H_2/100 km)	0.748	0.763	0.781
Mean stack power (kW)	6.88	3.95	4.24
Peak stack power (kW)	31.56	37.03	36.50
Battery SOC (start → end, %)	80.0 → 79.1	80.0 → 83.7	80.0 → 85.6

[Downloaded from rds.iust.ac.ir on 2026-11-15]

3.1 Driving-cycle speed profiles

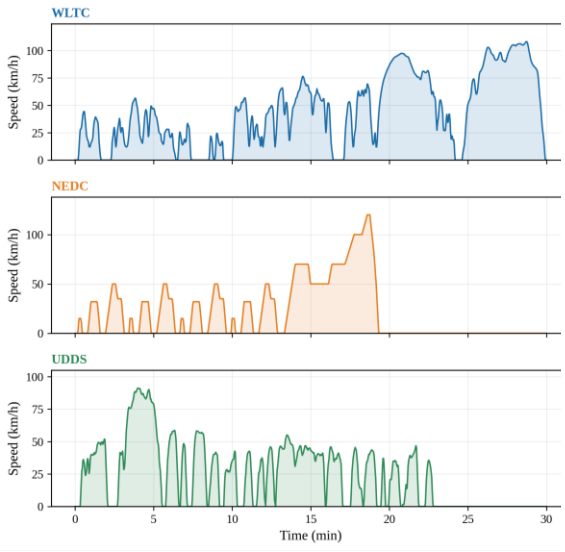


Figure 3: Vehicle speed profiles for the three simulated driving cycles: (top) WLTC, (middle) NEDC, (bottom) UDDS.

Figure 3 presents the speed trace of each driving cycle. The WLTC exhibits its characteristic four-phase structure (low, medium, high and extra-high speed segments), the longest test duration among the three cycles (30 min), and the most severe sequence of accelerations and decelerations, culminating in a peak speed of 108.1 km/h during the final phase. The NEDC, by contrast, displays its well-known stepped profile consisting of four repetitions of the Urban Driving Cycle (UDC) followed by the Extra-Urban Driving Cycle (EUDC) segment, which reaches a constant 120 km/h; the mild, quasi-steady acceleration ramps make the NEDC the least transient-severe of the three cycles. The UDDS reproduces stop-and-go urban traffic punctuated by a short semi-highway segment between minutes 3 and 5, with a maximum speed limited to 91.2 km/h. These fundamental differences in duration, acceleration severity and mean speed (44.5 km/h for WLTC, 33.6 km/h for NEDC and 31.7 km/h for UDDS, all averaged over moving time) underlie the differences in hydrogen consumption and

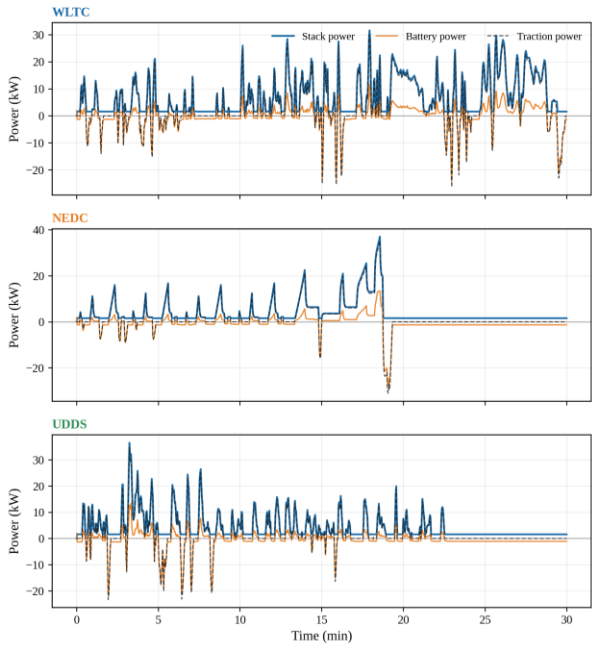


Figure 4: Traction, stack and battery power traces for the three driving cycles, illustrating the power-split behaviour of the hybrid fuel-cell powertrain.

power-management behaviour discussed in the following subsections.

3.2 Power-split strategy between the fuel-cell stack and the battery

Figure 4 shows the traction power, fuel-cell stack power and battery power simultaneously for each cycle. A distinctive and physically consistent feature is that, over essentially every interval of positive traction demand, the stack-power trace (blue) closely tracks the traction-power trace (dashed), indicating that the fuel-cell stack operates as the primary, base-load power source, while the battery contributes only a comparatively small share to cover instantaneous load fluctuations. This behaviour recurs across all three cycles, but its intensity scales with cycle dynamics: under the sharper, more frequent accelerations of the WLTC, battery power swings between −11.5 kW and −24.1 kW during regenerative events, whereas

[Downloaded from rds.iust.ac.ir on 2026-11-15]

the milder NEDC ramps produce a narrower excursion range.

The most notable finding in Fig. 4 concerns regenerative braking (negative traction demand): the stack power never drops below its baseline of roughly 1.5–2 kW (associated with balance-of-plant and auxiliary loads) and does not accept reverse power flow, whereas the entire recovered braking energy is absorbed by the battery, whose power reaches as low as −28.1 kW under NEDC. This confirms that the energy-management strategy implemented in the model protects the stack from reverse power flow and delegates regenerative-energy management entirely to the battery subsystem a strategy consistent with the physical constraints and durability considerations of PEM fuel-cell stacks used in production FCEVs such as the Toyota Mirai.

3.3 Hydrogen consumption and tank depletion

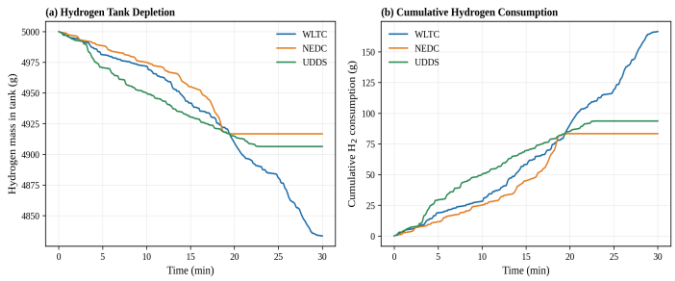


Figure 5: (a) Hydrogen mass remaining in the tank and (b) cumulative hydrogen consumption over time for the three driving cycles.

Figure 5(a) shows the depletion of hydrogen mass in the tank, and Fig. 5(b) shows the corresponding cumulative consumption. Because the NEDC and UDDS cycles are shorter than the WLTC, their curves plateau at approximately 19.5 min and 22.7 min, respectively, once the vehicle comes to rest, whereas the WLTC continues to consume hydrogen throughout the full 30-minute duration and therefore records the highest cumulative consumption, 166.52 g nearly twice that of the NEDC (83.34 g). The slope of the cumulative-consumption curve steepens markedly during the aggressive acceleration events of the WLTC high- and extra-high-speed phases (after minute 20), consistent with the corresponding rise in stack power demand in those regions.

A noteworthy observation in Fig. 5(b) is that, despite the clear differences in instantaneous consumption rate, the overall slopes of the three curves converge over the medium term. This observation anticipates the key result of Section 3.6, namely that the mass-specific hydrogen economy of the three cycles differs only marginally.

3.4 Battery state-of-charge trajectory

Table 4 summarises the battery state-of-charge (SOC) behaviour recorded for each driving cycle. In all three cases, the battery started from an identical initial condition of 80% SOC and ended the test within a comparatively narrow band of 79.1–85.7%, confirming that the energy-management strategy keeps the battery close to its nominal operating window regardless of the imposed driving cycle. The WLTC is the only cycle that ends with a net SOC deficit (−0.87 percentage points), consistent with its longer duration and higher cumulative energy throughput, whereas the shorter NEDC and UDDS cycles both end with a net SOC surplus (+3.66 and +5.65 percentage points, respectively), indicating that these cycles terminate while the battery is still in a charge-recovery phase following the transient loads encountered earlier in the trace.

[Downloaded from rds.iust.ac.ir on 2026-11-15]

Table 4: Battery state-of-charge (SOC) statistics for the three driving cycles.

Driving cycle	Initial SOC (%)	Final SOC (%)	Net ΔSOC (p.p.)	Minimum SOC (%)	Maximum SOC (%)
WLTC	80.00	79.13	−0.87	72.39	90.98
NEDC	80.00	83.66	+3.66	73.02	86.63
UDDS	80.00	85.65	+5.65	77.39	87.32

The minimum-SOC column reveals that the largest transient depth of discharge occurs under the NEDC (a drop to 73.02%, i.e. 6.98 percentage points below the initial value), despite this cycle having the mildest average acceleration profile of the three (Fig. 4); this reflects the single, sharp high-power event associated with the EUDC segment rather than the cycle's overall severity. The WLTC, by contrast, reaches the highest maximum SOC (90.98%), reflecting its more frequent and evenly distributed regenerative-braking events that repeatedly recharge the battery throughout the longer test duration. Overall, the SOC excursions listed in Table 4 remain within a physically reasonable and charge-sustaining range for all three cycles, supporting the robustness of the underlying power-split strategy discussed in Section 3.2.

3.5 Estimated vehicle range

Table 5 reports the estimated remaining driving range for each cycle, evaluated once the range estimator's initial transient has settled ($t \geq 2$ min). The mean estimated range lies within a relatively narrow band of 584.6–631.9 km across the three cycles, consistent with the nominal 5 kg hydrogen tank capacity and the overall system efficiency discussed in Section 4.6. The UDDS cycle yields both the highest maximum range (739.4 km) and the highest mean range (631.9 km) among the three cycles, reflecting its lower average speed and milder acceleration severity and therefore its more favourable instantaneous efficiency (Section 4.1). The WLTC and NEDC show comparable mean ranges (584.6 km and 615.1 km, respectively), but the NEDC exhibits the widest overall spread between its minimum and maximum values (403.8–680.9 km), which mirrors the sharp, single high-power transient identified in the SOC data (Table 5) and the abrupt final acceleration/deceleration sequence of its EUDC segment (Fig. 4).

Comparing the initial and final range estimates in Table 4 further illustrates the difference in net energy balance among the cycles: the range estimate increases from start to end for both WLTC (537.06 → 667.23 km) and NEDC (498.34 → 652.54 km), consistent with the improving battery SOC trend noted for these cycles in Section 4.4, whereas it decreases slightly for UDDS (735.55 → 635.41 km) despite the latter's positive net ΔSOC an apparent discrepancy that arises because the range estimator responds to the instantaneous hydrogen consumption rate rather than to the battery SOC alone, and therefore continues to reflect the cumulative depletion of the hydrogen tank even while the battery itself is being recharged. This distinction reinforces the importance of interpreting range and SOC as complementary, rather than interchangeable, indicators of the vehicle's remaining energy reserve.

Table 5: Estimated remaining vehicle range statistics for the three driving cycles.

Driving cycle	Initial range (km)	Final range (km)	Minimum range (km)	Maximum range (km)	Mean range (km)
WLTC	537.06	667.23	464.71	667.68	584.56
NEDC	498.34	652.54	403.85	680.91	615.10
UDDS	735.55	635.41	464.68	739.38	631.85

3.6 Comparative performance summary

[Downloaded from rds.iust.ac.ir on 2026-11-15]

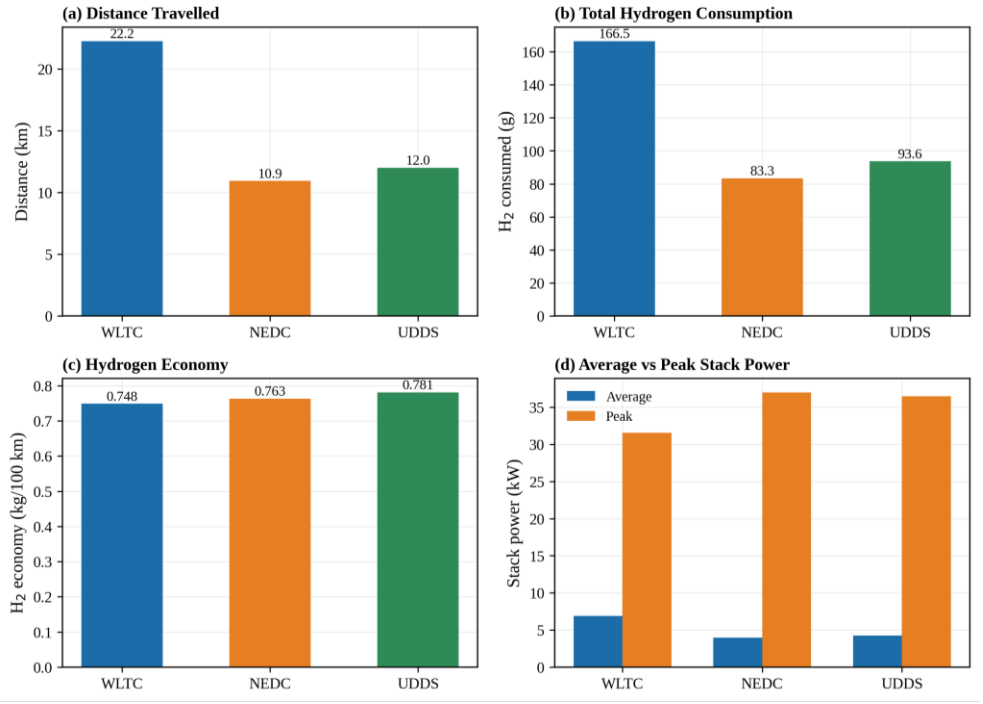


Figure 6: Comparative performance summary of the three driving cycles: (a) distance travelled, (b) total hydrogen consumption, (c) hydrogen economy, and (d) average versus peak stack power.

Figure 6 compares four key performance indicators across the three cycles. Panels (a) and (b) confirm that, owing to the difference in distance travelled, the WLTC accounts by far for the largest distance (22.25 km) and the largest absolute hydrogen consumption (166.52 g). The more significant finding, however, appears in panel (c): once consumption is normalised by distance (hydrogen economy, expressed in kg per 100 km), the differences among the three cycles narrow substantially, converging to a tight range of 0.748–0.781 kg/100 km a relative spread of less than 5%. This result indicates that, despite pronounced differences in speed profile, acceleration severity and duration, the implemented energy-management strategy sustains a comparatively stable efficiency that is largely independent of cycle type, a property generally regarded as an indicator of a robust energy-management strategy in hybrid fuel-cell vehicles. Notably, the UDDS shows the least favourable hydrogen economy of the three despite its lower average speed; this may be attributed to its high frequency of stop-and-go events and the reduced fuel-cell efficiency typically associated with repeated partial-load cycling.

Panel (d) further shows that, although the mean stack power differs considerably across cycles (6.88 kW for WLTC versus 3.95 kW for NEDC and 4.24 kW for UDDS), the peak stack power remains within a comparatively narrow band of 31.6–37.0 kW for all three. This convergence in peak power indicates that the fuel-cell stack's capacity to respond to short-term transient power demand is exploited similarly regardless of cycle type, whereas the difference in mean power is primarily a consequence of each cycle's duty cycle that is, its ratio of moving time to idle time.

[Downloaded from rds.iust.ac.ir on 2026-11-15]

3.7 Summary

The simulation results demonstrate that the fuel-cell propulsion system exhibits consistent and predictable energy-management behaviour across all three standard driving cycles considered: the fuel-cell stack operates as the primary power source, while the battery acts as a dynamic buffer that absorbs regenerative braking energy and covers transient peak-power demands. Despite substantial differences in speed profile and transient severity among the WLTC, NEDC and UDDS cycles, the hydrogen economy of the system remains stable within a narrow band centred around 0.75 kg per 100 km, indicating the robustness of the implemented control strategy. These findings are consistent with reported field performance of production fuel-cell vehicles such as the Toyota Mirai and support the validity of the Amesim simulation model for future energy-management optimisation studies.

4. Conclusions

This study presented a system-level, forward-facing simulation framework for a Toyota-Mirai-type fuel-cell electric vehicle and evaluated its energy-conversion and power-management behavior under three standardized driving cycles with markedly different dynamic characteristics. The comparative, like-for-like analysis leads to the following conclusions:

- The fuel-cell stack consistently operates as the primary, base-load power source across all three driving cycles, closely tracking traction-power demand under positive-load conditions.
- The traction battery functions as a dynamic energy buffer, absorbing the entirety of regenerative-braking energy and covering short-duration transient peak-power demands, while the stack is fully protected from reverse power flow.
- Absolute hydrogen consumption and mean stack power differ substantially among cycles (largest under WLTC due to its longer duration and higher transient severity), reflecting differences in duty cycle rather than differences in control effectiveness.
- Once normalized by travelled distance, hydrogen economy converges to a narrow band (0.748–0.781 kg H2/100 km), and peak stack power remains confined to 31.6–37.0 kW regardless of cycle type, indicating that the implemented energy-management strategy achieves cycle-independent efficiency and stable component utilization.
- Battery SOC and estimated driving range remain within physically reasonable, charge-sustaining bounds for all cycles, confirming the robustness of the power-split strategy under both mild (NEDC) and highly transient (WLTC) demand profiles.
- The developed Amesim-based model provides a physically transparent, validated baseline suitable for extension toward optimization-based, real-world, and degradation-aware energy-management studies for fuel-cell/battery hybrid powertrains.

List of Symbols

Symbol	Description
A_f	Frontal area
C_d	Aerodynamic drag coefficient
C_r	Rolling-resistance coefficient
D	Distance travelled
F_{aero}	Aerodynamic-drag force
F_{grade}	Grade-resistance force
F_{in}	Inertial force
F_{roll}	Rolling-resistance force
F_{trac}	Total tractive force
g	Gravitational acceleration
HE	Hydrogen economy
I_{bat}	Battery current
I_{stack}	Fuel-cell stack current

[Downloaded from rds.iust.ac.ir on 2026-11-15]

Symbol	Description
LHV_{H2}	Lower heating value of hydrogen
m	Vehicle mass
$\dot{m}_{H2}$	Hydrogen mass-flow rate
$m_{H2,cons}$	Cumulative hydrogen mass consumed
P_{bat}	Battery power
P_{BoP}	Balance-of-plant power demand
$P_{conv,loss}$	Converter and drivetrain power losses
P_{dem}	Electrical power demand
$P_{FC,net}$	Net fuel-cell-system power
P_{stack}	Fuel-cell stack power
$\bar{P}_{stack}$	Mean fuel-cell stack power
$P_{stack,peak}$	Peak fuel-cell stack power
P_{wheel}	Instantaneous wheel power
Q_{nom}	Nominal battery charge capacity
SOC	Battery state of charge
SOC_0	Initial battery state of charge
T	Total cycle duration
$v(t)$	Vehicle speed
V_{stack}	Fuel-cell stack voltage

Greek symbols

Symbol	Description
ΔSOC	Net change in battery state of charge
η_{FC}	Fuel-cell energy-conversion efficiency
θ	Road inclination angle
ρ_{air}	Air density

List of Abbreviations

Abbreviation	Full form
BoP	Balance of Plant
DC	Direct Current
EMS	Energy-Management Strategy
EUDC	Extra-Urban Driving Cycle
FCEV	Fuel-Cell Electric Vehicle
FTP-72	Federal Test Procedure 72
NEDC	New European Driving Cycle
PEMFC	Proton-Exchange-Membrane Fuel Cell
SOC	State of Charge
UDC	Urban Driving Cycle
UDDS	Urban Dynamometer Driving Schedule
WLTC	Worldwide Harmonized Light-Duty Vehicles Test Cycle

References

[1] J. Kurtz, S. Sprik, G. Saur, and S. Onorato, "Fuel Cell Electric Vehicle Driving and Fueling Behavior," 2018, Accessed: Jul. 09, 2026. [Online]. Available: https://www.nrel.gov/docs/fy19osti/73010.pdf.

[2] I. S. Sorlei *et al.*, "Fuel Cell Electric Vehicles—A Brief Review of Current Topologies and Energy Management Strategies," *Energies 2021, Vol. 14, Page 252*, vol. 14, no. 1, p. 252, Jan. 2021, doi: 10.3390/EN14010252.

[3] V. Mounica and Y. P. Obulesu, "Hybrid Power Management Strategy with Fuel Cell, Battery, and Supercapacitor for Fuel Economy in Hybrid Electric Vehicle Application," *Energies 2022, Vol. 15, Page 4185*, vol. 15, no. 12, p. 4185, Jun. 2022, doi: 10.3390/EN15124185.

[4] S. Mansour and M. Raeesi, "Performance assessment of fuel cell and electric vehicles taking into account the fuel cell degradation, battery lifetime, and heating, ventilation, and air conditioning system," *Int. J. Hydrogen Energy*, vol. 52, pp. 834–855, Jan. 2024, doi: 10.1016/J.IJHYDENE.2023.05.315.

[5] M. Carignano and R. Costa-Castelló, "Toyota Mirai: Powertrain Model and Assessment of the Energy Management," *IEEE Trans. Veh. Technol.*, vol. 72, no. 6, pp. 7000–7010, Jun. 2023, doi: 10.1109/TVT.2023.3237173.

[6] U. Usmanov, S. Ruzimov, A. Tonoli, and A. Mukhitdinov, "Modeling, Simulation and Control Strategy Optimization of Fuel Cell Hybrid Electric Vehicle,"

[Downloaded from rds.iust.ac.ir on 2026-11-15]

Vehicles 2023, Vol. 5, Pages 464-481, vol. 5, no. 2, pp. 464–481, Apr. 2023, doi: 10.3390/VEHICLES5020026.

[7] F. Calise *et al.*, "Effect of the Degree of Hybridization and Energy Management Strategy on the Performance of a Fuel Cell/Battery Vehicle in Real-World Driving Cycles," *Energies 2024, Vol. 17, Page 729*, vol. 17, no. 3, p. 729, Feb. 2024, doi: 10.3390/EN17030729.

[8] S. Changizian, P. Ahmadi, M. Raeesi, and N. Javani, "Performance optimization of hybrid hydrogen fuel cell-electric vehicles in real driving cycles," *Int. J. Hydrogen Energy*, vol. 45, no. 60, pp. 35180–35197, Dec. 2020, doi: 10.1016/J.IJHYDENE.2020.01.015.

[9] Y. Sun, C. Xia, B. Yin, Y. Yu, J. Han, and H. Gao, "Adaptive Energy Management Strategy of Fuel Cell Electric Vehicle," *International Journal of Automotive Technology 2022 23:5*, vol. 23, no. 5, pp. 1393–1403, Oct. 2022, doi: 10.1007/S12239-022-0122-Y.

[10] M. A. Islam, I. Jahan, and O. Farrok, "Fuel cell hybrid electric vehicle with real-world driving cycle: six-step control strategy for dynamic energy management and fuel optimization," *Energy Conversion and Management: X*, vol. 29, p. 101435, Jan. 2026, doi: 10.1016/J.ECMX.2025.101435.

[11] M. Iqbal, A. Benmouna, and M. Becherif, "Data-Driven Modelling and Simulation of Fuel Cell Hybrid Electric Powertrain," *Hydrogen 2025, Vol. 6, Page 53*, vol. 6, no. 3, p. 53, Aug. 2025, doi: 10.3390/HYDROGEN6030053.

[12] D. C. Da Silva, L. Kefsi, and A. Sciarretta, "Closed-Form Expression to Estimate the Hydrogen Consumption of a Fuel Cell Hybrid Electric Vehicle," *IEEE Trans. Veh. Technol.*, vol. 73, no. 4, pp. 4717–4728, Apr. 2024, doi: 10.1109/TVT.2024.3350351.

[13] B. M. Alves, P. Savignac, and P. Leduc, "Energy balance and hydrogen exhaust emissions of the second-generation Toyota Mirai," *Int. J. Hydrogen Energy*, vol. 156, p. 150411, Aug. 2025, doi: 10.1016/J.IJHYDENE.2025.150411.

[14] W. Cieslik, A. Stolarski, and S. Freda, "Electricity Energy Flow Analysis of a Fuel Cell Electric Vehicle (FCEV) Under Real Driving Conditions (RDC)," *Energies 2025, Vol. 18, Page 6458*, vol. 18, no. 24, p. 6458, Dec. 2025, doi: 10.3390/EN18246458.

[15] M. M. Davari, J. Jerrelind, and A. Stensson Trigell, "Energy efficiency analyses of a vehicle in modal and transient driving cycles including longitudinal and vertical dynamics," *Transp. Res. D Transp. Environ.*, vol. 53, pp. 263–275, Jun. 2017, doi: 10.1016/J.TRD.2017.04.019.

[16] M. A. Zakizadeh, A. A. Laleh, and M. Mollajafari, "Adaptive ensemble ANFIS-based energy management strategy for fuel cell hybrid electric vehicles," *Energy Reports*, vol. 16, p. 109714, Dec. 2026, doi: 10.1016/J.EGYR.2026.109714.

[Downloaded from rds.iust.ac.ir on 2026-11-15]